Artigo de Pesquisa

Correlations between landslide scars parameters using remote sensing methods in the estrada de ferro Vitória-Minas, southeastern Brazil

Correlações entre parâmetros de cicatrizes de deslizamento utilizando sensoriamento remoto na estrada de ferro Vitória-Minas, sudeste do Brasil

Denise de Fátima Santos da Silva [1], **Rosyelle Cristina Corteletti** [2], **Roberto Almeida Cunha Filgueiras** [3] e **Allan Erlikhman Medeiros Santos** [4]

[1] Universidade Federal de Minas Gerais, Centro de Pesquisa Professor Manoel Teixeira da Costa, Belo Horizonte, Brasil.
denisefss@yahoo.com.br.
ORCID: https://orcid.org/0000-0002-9695-2449

[2] Universidade Federal de Ouro Preto, Núcleo de Geotecnia da Escola de Minas, Ouro Preto, Brasil.
rosyelleccorteletti@gmail.com.
ORCID: https://orcid.org/0000-0001-6006-2877

[3] GERPRO – Gerenciamento de Projetos S/C Ltda, Belo Horizonte, Brasil.
roberto@filgueiras.com.br.
ORCID: https://orcid.org/0000-0003-4391-9415

[4] Centro Federal de Educação Tecnológica de Minas Gerais, Departamento de Minas e Construção Civil, Araxá, Brasil.
allanerlikhman@cefetmg.br.
ORCID: https://orcid.org/0000-0003-1241-8423

Resumo: O sensoriamento remoto tem sido largamente aplicado em estudos que envolvem registros e monitoramento de movimentos de massa, além disso, essas ferramentas são muito empregadas na geração de mapas de áreas de risco geológico. Neste artigo utilizou-se duas metodologias de sensoriamento remoto para identificação, caracterização e catalogação das cicatrizes geradas por deslizamento ao longo da Estrada de Ferro Vitória-Minas (EFVM). A primeira metodologia permitiu estimar a área e o volume das cicatrizes de deslizamento da EFVM por meio das imagens disponíveis no Google Earth Pro. A segunda metodologia utilizou-se de um drone para captação dos parâmetros em campo das cicatrizes de deslizamento. A partir dos parâmetros obtidos pode-se comparar as estimativas de áreas e volumes de deslizamentos pelo imageamento com drone com os dados obtidos a partir das imagens do Google Earth Pro e testar a aplicabilidade de ambos os métodos. Os resultados obtidos apontam estimativas de áreas de cicatrizes com correlação de 0,92 para as duas metodologias. Já as estimativas de volume apresentaram correlação 0,8; com subestimativa dos resultados obtidos por meio do Google Earth Pro.

Palavras-chave: Cicatriz de deslizamentos; Google Earth Pro; Drone.

Abstract: The remote sensing has been widely used in studies involving records and monitoring landslides, also, this tool is widely used in mapping areas of geological risk. In this paper, two remote sensing methodologies were used to identify, characterize and catalog scars generated along the Estrada de Ferro Vitória-Minas (EFVM). The first methodology allowed to estimate the area and volume of landslides scars of EFVM through the images available in Google Earth Pro. The second methodology used a drone to capture the parameters in the field of landslides scars. From the obtained parameters it was possible to compare the estimates of areas and volumes of landslides by drone image with the data obtained by images of Google Earth Pro and to test the applicability of both methods. The results obtained showed estimates scars areas with

correlation of 0.92 for the two methodologies. The volume estimates presented a correlation of 0.8; with underestimation of the results obtained by Google Earth Pro.

Keywords: Landslide scars ; Google Earth Pro ; Drone.

1. Introduction

Natural disasters associated with landslides on natural slopes occur frequently throughout the world and have different causes and may be either singular or combined. Landslides reflect landscape instability that evolves over meteorological and geological timescales, and they also pose threats to people, property, and the environment (IVERSON et al., 2015). Thus, the need to predict these events is justified. However, the prediction methods are still a great challenge in geotechnical engineering, due to the many variables involved in this phenomenon.

In linear works such as highways or railways, for example, studies on the prediction of the area and the volume of sliding mass are extremely complex and assume particularly relevant characteristics. These characteristics are due to the nature of the project, where there is a wide trajectory crossing different geological sites, with different geological, geotechnical, topographic and vegetation characteristics (CORTELETTI, 2017; SILVA et al., 2018).

In the case of railroad embankments, landslides, when reaching the domain of the railway platform, can affect the railroad in several ways, such as the traffic stoppage and the interdiction of the route by compromising the flow of loads and/ or passengers (CORTELETTI, 2017). The severity of these disorders largely depends on landslide speed and travel distance, which are collectively described as landslide "mobility" (IVERSON et al., 2015). Landslide size controls the destructive power of landslides and is related to the frequency of occurrence, with larger landslides being less frequent than smaller ones (VALAGUSSA et al., 2019). For this reason, knowing the number, area and volume of landslides makes it possible to establish the hierarchy of susceptible slopes and thus to assess the risk of landslides (GUZZETTI et al., 1999; CARDINALI et al., 2002; MALAMUD et al., 2004; REICHENBACH et al., 2005; GUZZETTI et al., 2009).

Landslides analyzes are performed from inventories. These inventories allow correlations between the record of past landslides in a given area and the conditioning factors, such as lithological and topographic structures (GUTHRIE, 2002; AVANZI; GIANNECCHINI; PUCCINELLI, 2004), the type of use (LEE; CHWAE; KYUNGDUCK, 2002; PEROTTO-BALDIVIEZO et al., 2004) and the specific trigger mechanism (GUNS; VEERLE, 2014). The area of a landslide can be determined from maps in digital format, as can be seen (GUZZETTI et al., 2005, IMAIZUMI; SIDLE, 2007; GALLI et al., 2008), where area and density of landslides may be calculated for different periods.

Determining the volume of a landslide is a more difficult task that requires information on the surface and sub-surface geometry of the slope failure (GUZZETTI et al., 2009). Some authors estimate the volume of a slip simply by assuming that the surface of a slip is half of an ellipsoid (CRUDEN; VARNES, 1996).

By using empirical relationships, it is possible to link the volume of individual landslides to the geometric measurements of the failures, such as the area of landslide (SIMONETT, 1967; RICE et al., 1969; INNES, 1983; HOVIUS; STARK; ALLEN, 1997; GUTHRIE; EVANS, 2004; Korup, 2005b; TEN BRINK; GEIST; ANDREWS, 2006; IMAIZUMI; SIDLE, 2007; GUZZETTI et al., 2008; IMAIZUMI; SIDLE; KAMEI, 2008; GUZZETTI et al., 2009; SILVA et al., 2018). Through the relationships it is possible to evaluate and delimit areas of risk, to assist in the immediate applications of decision making in relation to the planning and prioritization of works, besides allowing the coexistence with these types of phenomenon (POLANCO, 2010, SILVA et al., 2018).

In recent years, drones equipped with cameras to perform digital aerial photogrammetry, have gained market share, mainly because of the ease of data acquisition and the amount of information an aerial image can provide. Currently, drones have integrated field positioning technologies to generate high accuracy and precision products for pre-projects in the various fields of engineering, agriculture and landslides studies (TURNER et al.,, 2015; ROSSI et al., 2016; PETERNEL et al.,, 2017; PEPPA et al.,, 2017; BALEK; BLAHUT, 2017; GUPTA; SHUKLA, 2018; ROSSI et al., 2018; GARCIA-DELGADO; MACHUCA; MEDINA, 2019).

In this paper, a quadcopter drone equipped with a 12-megapixel camera was used to acquire photogrammetric data on the VALE S.A. railway line, which is located in the southeastern region of Brazil, in the

Estrada de Ferro Vitória-Minas (EFVM) line. Eighteen landslides were cataloged for which area and volume measurements were estimated. The objective of this study was to test the applicability and validate the results of the estimates made in eighteen scars through Google Earth Pro and compare them with the estimates made in drone imaging, determining the relation between the area and volume variables, in addition to the creation of high resolution 3D surface models for better characterization of EFVM scars.

1.1 Use of remote sensing for study and mapping of landslides

Remote sensing is applied in studies involving logging and monitoring of landslides and is also widely used in generating maps for areas of geological risk, as can be seen in Guzzetti et al. (2012), Fan et al. (2018) e Karki et al. (2018). However, Vanacôr (2006) draws attention to the fact that the interpretation of landslides from remote sensing requires knowledge of the distinct structures associated with slope movement and image characteristics. Thus, an adequate interpretation depends on the spatial resolution of the image, which, if very low, makes it difficult to identify or recognize the features.

According to Vanacôr (2006) the interpretation of features in an image is influenced by what exists between the features and their surroundings. Thus, the identification of slides depends on the contrast of the spectral or spatial differences between the mass movement and its surroundings. In addition, the identification of such movements is directly affected by the period since the failure, due to erosive processes, besides the vegetation recomposition.

The use of remote sensing for the study and mapping of mass movements is performed from the direct detection (scars originated by the processes). Scars are characterized by the removal of the vegetation cover and exposure of superficial layers of the soil, in addition to the material transported and deposited in the form of a range of debris. Indicators can be observed through changes in vegetation cover (different densities and vegetation types due to previous landslides), soil use (removal of vegetation by anthropic action in areas prone to landslides or road cutting) and hillside (VANACÔR, 2006).

According to Mendonça (2012) the use of orbital images obtained on dates close to the event is an important product for the elaboration of scars inventories. More accurate mapping of scars is critical for the methods of susceptibility and slope hazard investigation/analysis, as they allow calibration and validation of such methods.

1.1.1. Google Earth Pro as a tool to building landslide scars inventory

In actual practice, high-resolution satellite imagery is extremely widespread. Google Earth has revolutionized the way we look at landscapes, as well as familiarizing the user with satellite imagery. Recently, high spatial resolution images were integrated in this large mosaic, allowing for more detailed observations. In the absence of financial resources to acquire aerial photographs or satellite images, it is possible to work with existing ones in Google Earth (PANIZZA; FONSECA, 2011). In addition, Google Earth has been used in archaeological studies as can be seen in Kennedy and Bishop (2011); Parcak (2009); Sadr and Rodier (2012) and in landslides studies (SILVA et al., 2018).

The Google Earth database consists of a set of images from sensors of various resolutions arranged to form a continuous image of the entire planet. In addition, high resolution images of Google Earth are preferably from prominent regions, such as areas of high population density, tourist regions and attractive regions of the world. These images come from various distributors and are changed periodically. Therefore, an image viewed today in Google Earth can be replaced with a newer image without any notification (LOPES, 2009).

1.1.2. Use of drones to characterize landslides

With the popularization of drones, photogrammetric products have gained space in the market, for reasons such as the ease of data acquisition and the amount of information that an aerial image can offer. In practice, drones have integrated ground-positioning technologies to generate high-precision products for pre-projects in areas such as engineering, agriculture and services. According to Chang-Chun et al. (2011), drones have the following advantages: real-time applicability, flexible search planning, high resolution, low cost and power to collect information in hazardous environments without risk.

Currently there is a great facility for the acquisition or assembly of a drone, for aerial photogrammetry purposes, from various ready-made models, parts and components available in the market. Despite the high

technology, a complete system has a significantly lower cost when compared to a conventional aerial photogrammetric system (SILVA et al., 2014). Due to this accessibility to the public, its application in the mapping of small areas with few hectares has grown very much today (SILVA et al., 2014). Among the applications are the mining, civil, urban and environmental engineering works, as well as surface modeling and monitoring (EISENBEISS; SAUERBIER, 2011, TRAVELLETTI et al., 2012, JAMES; ROBSON, 2012; COLOMINA; MOLINA, 2014; ROSSI et al., 2018).

2. Material and Methods

2.1. Study area: Estrada de Ferro Vitória-Minas (EFVM)

This research was developed to correlate estimated morphometrics data: area, shape and volume landslide scars in Google Earth Pro with estimated data through drone imaging. For this, we took as reference the trunk line of Estrada de Ferro Vitória Minas (EFVM). EFVM is one of the largest railroads in the world and has some of the best productivity rates.

EFVM is located in the southeastern region of Brazil, between Minas Gerais and Espirito Santos states, and it crosses 25 cities in both states. The railroad has 929 km of line extension (607 km of double line) and the trunk line has 540 km. EFVM handled 119.2 million tons of ore, as well as other cargo transported to other companies, such as coal and agricultural products. According to Vale (2017), EFVM transported almost one million people in 2014.

Silva et al., (2018) shows EFVM trunk line crosses several geological domains. The predominant lithologies are "granites", "gneisses", "gneisses with mafic intrusives", "metasedimentary rocks with presence of granitic intrusions", "shales and gneisses" and "unconsolidated sediments". Figure 1 shows the main road layout.

Figure 1. EFVM location.

2.2. Data estimate using Google Earth Pro

This study used the landslide scars inventory about EFVM was created by traversing 482 e 536 of the railroad through orbital images using the Google Earth Pro software. To identify the landslide scars, the altitude of the images point of view ranged from 2.55 kilometers to 368 meters, according to the level of detail needed to discriminate the scars. The final landslide scars inventory includes the stretch, location in UTM coordinates, the date of the image, and other characteristics such as area, shape and volume of the landslides.

In order to estimate the area of each delimited scar, the images for the 2016 year were extracted from Google Earth Pro. Then, the images were georeferenced in the ArcGis 10.3 software and the landslide scars areas were estimated. From ArcGis 10.3 were estimated areas 12 landslide scars in the EFVM.

The volume mobilized in the EFVM landslide scars in the present study was estimated using half of an ellipsoid as proposed by several authors, such as Cruden and Varnes (1996); Corrêa et al. (2009), Lee and Chi (2011) (Figure 2). The volume occurred in each lanslide was estimated according Eq. (1), considering the shape of half an ellipsoid, with semi-axes of the ellipse being: Vis, volume of material mobilized; Dd, scar depth; Wd, scar width e Ld, scar length. The increase in volume after displacement as a percentage of volume before displacement (swell factor) was not considered in the analyzes.

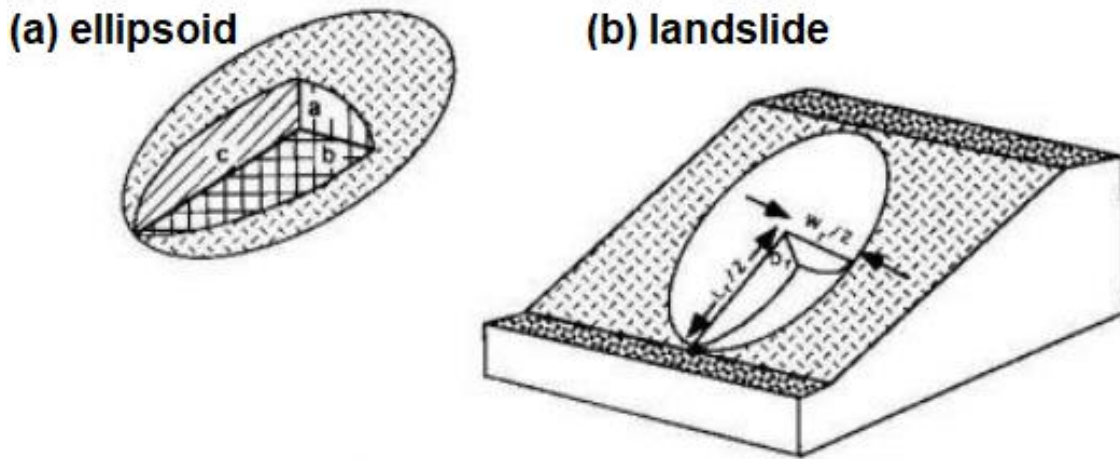$$V_{is} = \frac{1}{6} \pi D_d W_d L_d \qquad (1)$$

Figure 2. Estimated slide volume considering the shape of half an ellipsoid (Cruden and Varnes, 1996).

To obtain the semi-axes (length and width) of the ellipse, the Ruler tool of the Google Earth Pro software was used. The apparent depth of the failure (c1) was estimated from the elevation parameters that are reported by the program, using the Show Elevation Profile tool. Figure 3 schematically presents the methodology used to obtain the corrected failure depth (*d*).
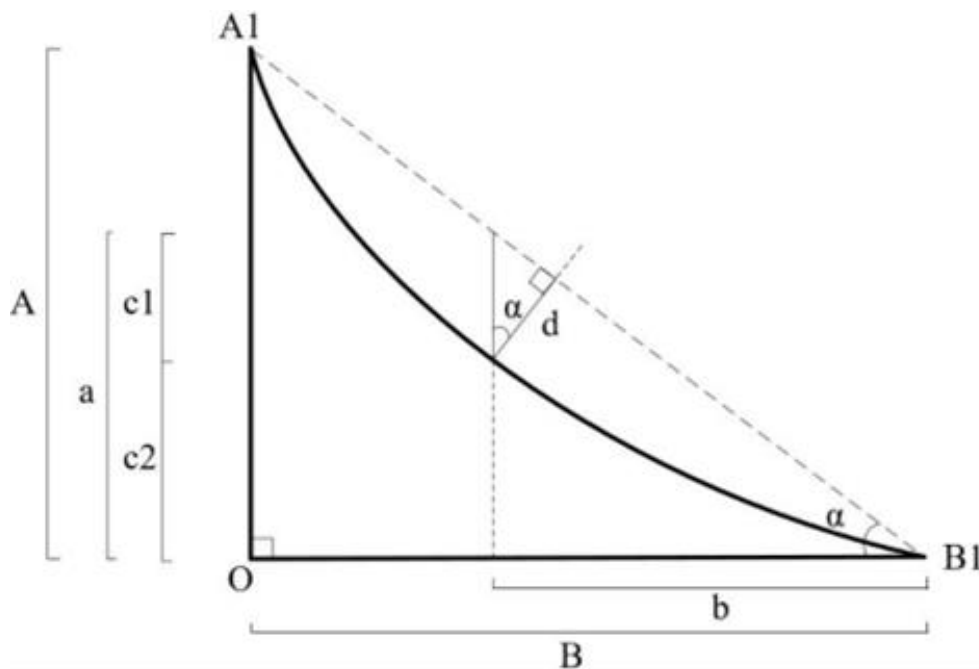

Figure 3. Methodology for obtaining the corrected failure depth.

The methodology used to obtain the corrected failure depth is explained below, using Eq.(2 to 6). In Figure 3, due to the similar triangles:

$$\frac{A}{a} = \frac{B}{b} \tag{2}$$

That is:

$$a = \frac{AB}{b} \tag{3}$$

From the value of a:

$$c1 = a - c2 \tag{4}$$

From the trigonometric relation:

$$cos\alpha = \frac{d}{c1} \tag{5}$$

So, this:

$$d = c1cos\alpha \tag{6}$$

Where d is the corrected depth of the landslide scar. It is worth mentioning that this corrected depth that is calculated is an estimate, as it is not real, since it does not consider the shape of the ground surface before the failure.

2.3 Data estimate using drone

For the purpose to validate the estimated data using Google Earth Pro, some of the landslide scars identified were verified in the field. Fieldwork was carried out between the 482 and 536 km stretches, and drone imaging estimated the area and volume of the lansdslide scars in the EFVM. For the acquisition of the images a quadcopter type drone (Figure 4) compact model Phanton IV with a resolution camera of 12 Mp (4000X3000 pixels) was used. The flight parameters used for imaging are shown in Table 1.

Figure 4. Drone used at work for data acquisition in the field.

Table 1. Determination of flight parameters for imaging of landslides scars.

Flights detail for scars registration of EFVM - Phanton IV												
Camera				CCD Size (mm)				Lens Focal Distance			Photo (pixel)	
Type		Description	Resolution	width		height		3,610			width	height
4		Phanton IV	12	6,317		4,738					4.000	3.000
Site	Height (m)	Length (m)		Width (m)		Extension (m)			GSD	Area (ha)		Photos		3D Densified
		L	n	W	n	Estimated	Real	Error	(cm/pixel)	Covered	Grid	Real	Model	Points
Area 01	110	329	5	194	8	3960,88	3826	0,034	7,62	25,99	6,38	254	254	13.246.266
Area 02	110	179	4	152	5	1945,66	1978	0,017	5,33	12,57	2,72	136	136	8.249.299
Area 04	110	443	5	208	10	5273,80	5410	0,026	4,51	23,83	9,21	326	279	16.876.787
Area 05	110	329	5	179	8	3826,08	3757	0,018	4,59	17,27	5,89	248	248	13.267.656
Area 06	110	277	7	194	5	3585,36	3546	0,011	7,98	26,01	5,37	226	226	11.435.569
Area 07	100	230	5	167	6	2720,47	2913	0,071	3,72	11,43	3,84	184	184	12.653.960
Area 08	100	273	4	119	7	2520,62	2594	0,029	4,07	11,42	3,25	172	172	10.710.315
Area 09	100	246	5	187	7	3157,01	3198	0,013	4,68	14,82	4,60	211	211	13.139.239
Area 10	100	276	4	132	7	2639,88	2545	0,036	4,25	12,01	3,64	178	173	10.356.095
Area 12	100	187	5	184	5	2379,69	2330	0,021	4,21	11,18	3,44	162	162	9.791.445
Area 13	100	231	5	144	6	2563,42	2510	0,021	4,61	14,90	3,33	175	175	10.319.889
Area 14	100	228	5	151	6	2592,94	2621	0,011	5,12	13,75	3,44	177	177	10.261.861

The flight was planned to cover a total of 64,586 ha of area at an altitude ranging from 100 to 110 m. The area presents characteristics considered difficult to process automatically, with uniform vegetation areas. After the flight, the images were processed in the software using 36 control points. In all imaged areas were generated orthomosaic, point cloud and digital surface models.

The flight plan was mapped in the Google Earth Pro software. In the field the process consisted of moving to a nearby clearing that served as a takeoff point to avoid contact with the propellers. A reference target was installed, the drone was positioned where the controlled takeoff took place that took the drone to an estimated height, and thus started the execution of the flight. The next step was to move it laterally at 90º over the area of interest. At the end of the imaging process, the drone was driven to landing.

2.4. Real-Time Kinematic (RTK)

In this work, the imaging was created simultaneously to the mapping using Real-Time Kinematic (RTK). For this, two receivers were used, continuously collecting data and a receiver used as a "base" that was installed in a reference station that had known coordinates. For real time position determination, the mobile receiver collects data at points of interest, also called control points. Figure 5 shows the equipment used to perform RTK geopositioning.

In the flights for acquisition of the data of this work, the equipment remained connected during the flights to allow the Ground Control Points (GCPs) of other areas to be deployed while performing the "previous" flights, those with demarcated points. In addition, precise point positioning (PPP) that is used for dynamically captured point correction (RTK) should have an approximate capture time of 4 hours.

Figure 5. Equipment used to perform RTK geopositioning.

2.5. Data processing

Terrain surface was estimated through drone aerophotogrammetry imaging and RTK geopositioning. Thus, the topography analyzed were used to more accurately estimate the scars studied in the EFVM, minimizing the degree of uncertainties imposed by the limitations of Google Earth images. In addition to improving the accuracy of estimates, obtaining parameters in the field allows obtaining a correction factor of the estimated variables through remote sensing.

Among the scars studied in the research, some were selected for field work. These scars were determined based on the accessibility of the exercises to perform the fieldwork. 12 stretches were selected, km 482 + 299, km 493 + 600, km 511 + 670, km 513 + 200, km 515 + 300, km 518 + 790, km 519 + 900, km 520 + 950, km 521 + 000, km 521 + 522, km 524+ 108, km 535 + 419. The names of the sections correspond to the kilometer of the point added to the meters, that is, km 482 + 299 means that the point is at kilometer 482,299. Some sections are added with the letters D or E, this means the margin in relation to the railway where the scar is located. The streches analyzed with their respective names can be seen in Figure 6.
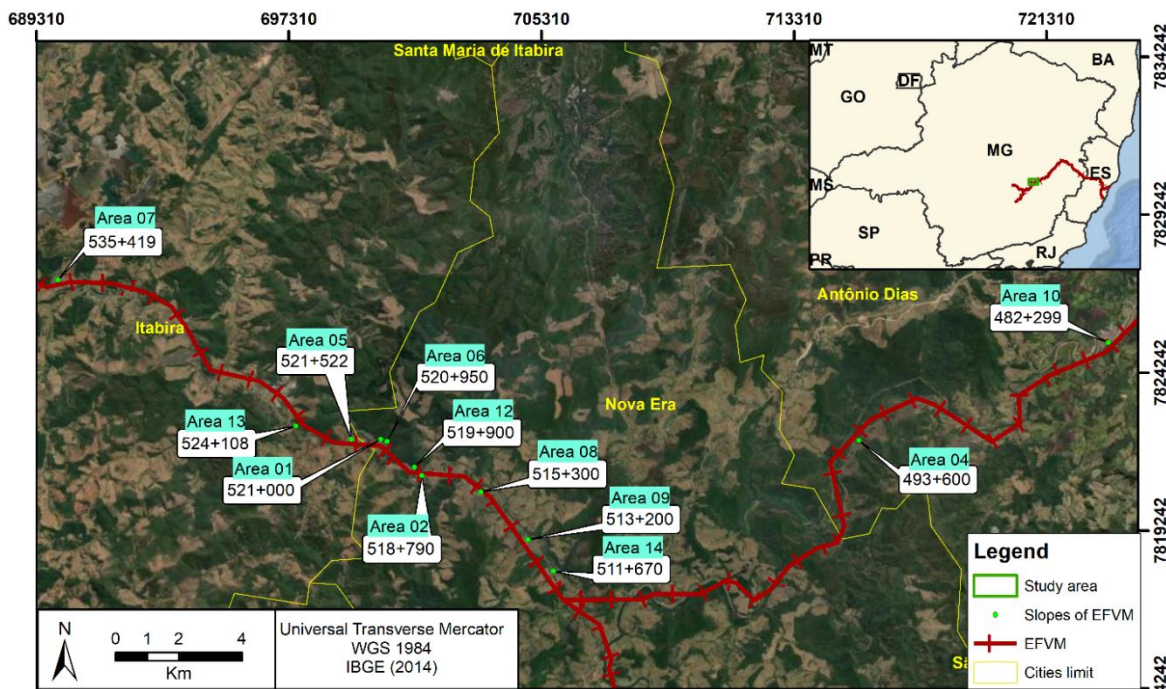

Figure 6. Location of the analyzed areas (in blue) with their respective stretches (in white) in EFVM.

To improve the accuracy of the generated orthomosaic in relation to the reference system UTM SIRGAS 2000, it was necessary to acquire control points in the field. For control points were marked using a "cross-shaped" arrangement of material PVC type for reference. Table 2 shows the reference base coordinates and the duration of the tracking for RTK.

Table 2. Duration of RTK screenings.

Data	Location	Time			UTM SIRGAS 2000 (m)		Orthometric altitude (m)
		Start	Finish	Duration	N	E	
17/01/17	Itabira	16:56:35	21:16:20	4:19:45	7.821.825,262	700.078,323	764,27
18/01/17	Itabira	10:42:55	15:30:25	4:47:30	7.821.825,271	700.078,335	764,26
19/01/17	Antônio Dias	11:16:40	14:26:45	3:10:05	7.821.780,269	715.227,230	473,67

First the images were processed in Pix4D software. Orthomosaic, point cloud and digital surface models were generated (Figure 7). The drone images needed to cover the study area and make the orthomosaics were 2889, with visible spectrum bands with 4000 x 3000 pixels (12 megapixels) for each image and spatial resolution ranging from 3.72 to 7.98 centimeters. To register the orthomosaic and to calculate the areas of the landslide scars, the software ArcGis 10.3 was used.
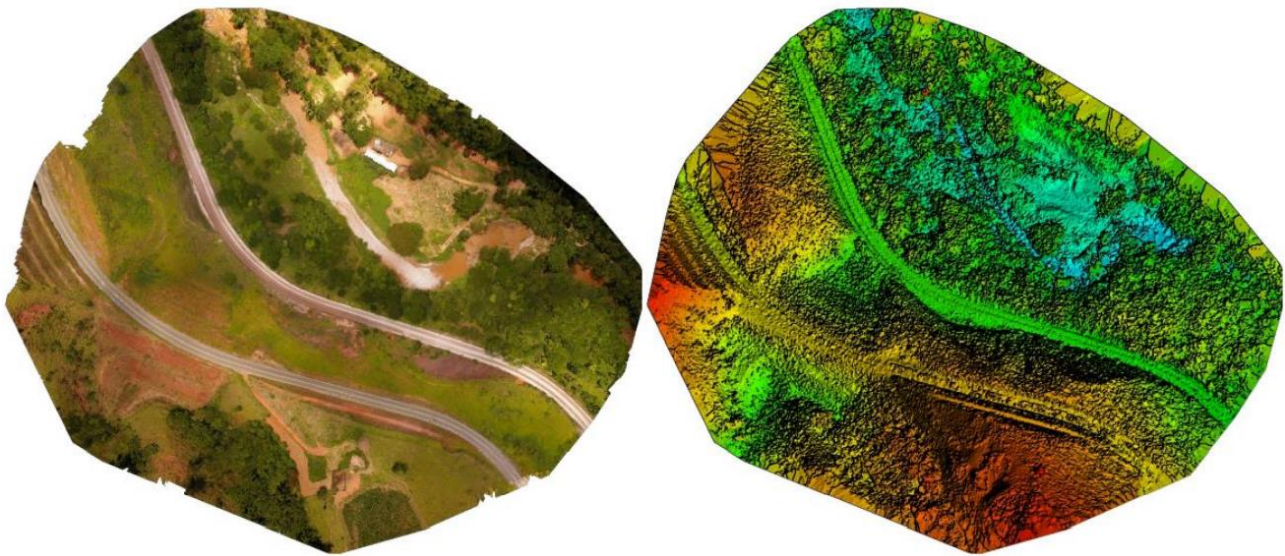
Figure 7. Orthomosaic and digital surface model (DSM) do trecho km 511+670 (Area 14) da EFVM.

The cartographic base, in DXF format on the 1:2000 cartographic scale, and relief data from the study area, obtained from aerophotogrammetric flight, were processed in the Global Mapper 17.0 software. Relief data is contour lines spaced from 0.2 to 0.5 meters and is in shapefile format used in the ArcGis. AutoCAD Civil 3D 2015 software was used to estimate field volumes. The volume estimate was performed so that the face of the slope before the event was a rectilinear curvature surface. Thus, the volume mobilized in the landslides was estimated by extracting the pre-event rectilinear topography from the topography of the current image. After the field, this data was processed and compared to the data estimated in Google Earth Pro.

3. Results and discussions

3.1. Landslide Scars characterization of EFVM

The scars analyzed in the EFVM field occur on soil or soil / rock slopes and according to CPRM (2000) are inserted in the Borrachudos Suite, Mantiqueira Complex and Guanhães Complex . Most landslide scars have no vegetation cover and many erosion grooves.

Some scars are located on residual soil slopes, as scar located at Km 519 + 900 (Area 12) as show Figure 8a. This scar presents the gneiss residual soil, with relic features of the original rock, as a banding characterized by the presence of the quartz and feldspar in the light portions and biotite and amphibole in the dark portions.
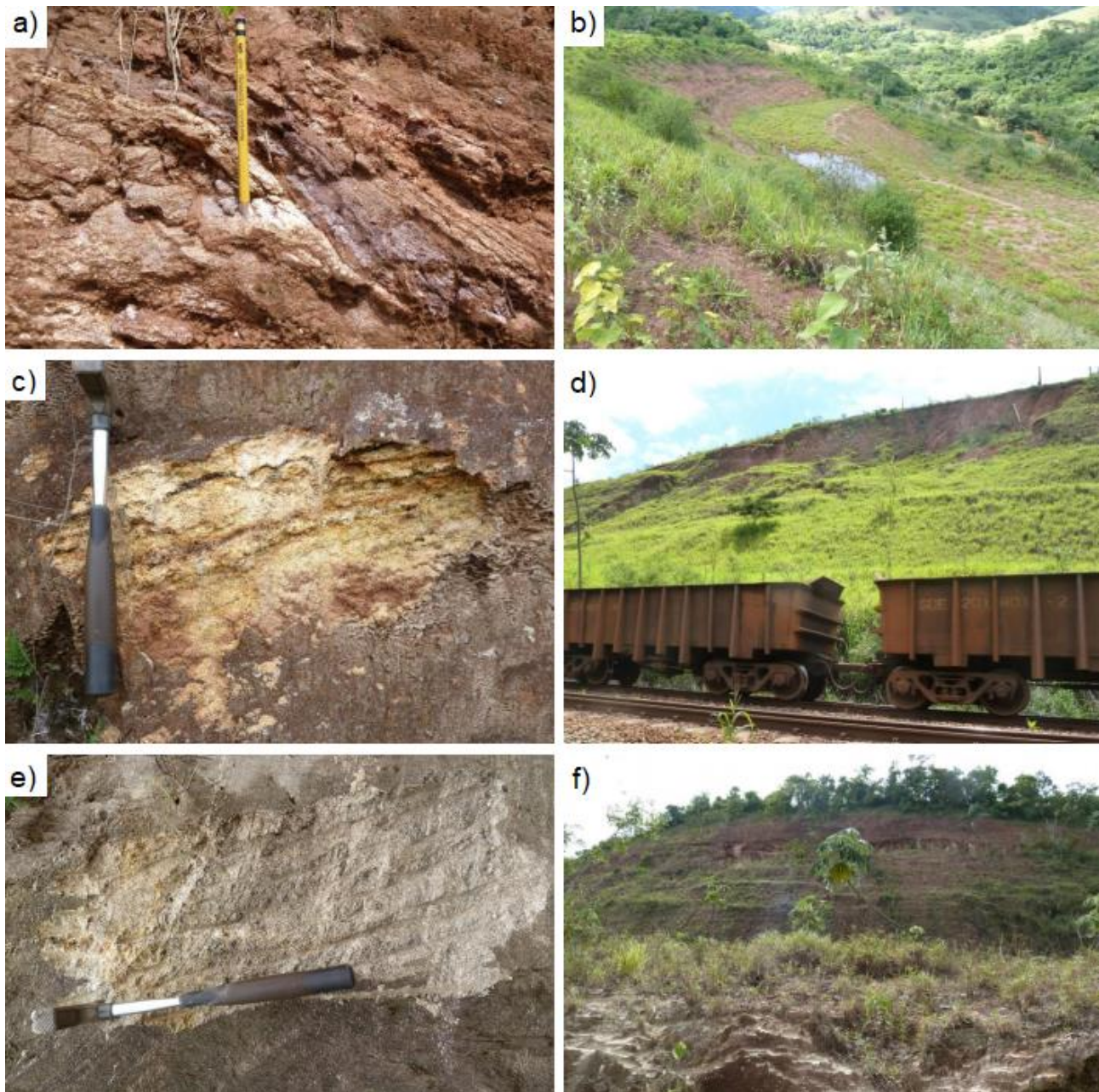
Figure 8. a) Residual soil that composing the embankment of the Km 519 + 900 (Area 12) strech inserted in the Borrachudos Suite. b) Accumulation of water on one of the benches in the slope area next to Km 511 + 670 (Area 14). c) Residual gneiss soil on the slope of Km 493 + 600 (Area 04). d) View of the Km 493 + 600 embankment and rotational landslide scar. e) Weathered granitoids from Km 482 + 299 (Area 10). f) View of the Km 482 + 299 slope.

As well as the scars from the Km 519 + 900 (Area 12) section, the scars from the Km 518 + 790 (Area 02) and Km 511 + 670 (Area 14) sections are inserted in the Guanhães Complex and have erosion grooves. In addition, no natural drainage lines or stabilization structures were observed. It was observed erosion points, undulations on the surface of the land and curved trees on the slopes. The scars showed cracks with an extension larger than 1 meter and an opening larger than 5 centimeters. In the near of Km 511 + 670 (Area 14) there was new slopes was build. In one of the benches on this new slope, there is a considerable amount of water accumulation, considering that on the inspection days there was no incidence of rain (Figure 8b).

At Km 515 + 300 (Area 08) is located a scar that presents a residual soil of gneiss (silty sandy) in transition with a red silty soil, which can be considered the gradual contact between the units of the Guanhães Complex and the Borrachudos Suite. The slope has erosion with grooves and it was observed needs for stabilization structures construction.

The slope located at Km 520 + 950 (Area 06) consists of soil / rock. The lower part of the massif consists of a granitoid of quartzitic composition from the Borrachudos Suite (CPRM, 2000). In the upper portion the massif is totally weathered. Erosion grooves was observed in the massif. It was observed needs to apply drainage systems, with the emergence of water located at the foot of the slope. Regarding stabilization structures, existing structures were observed, but these proved to be insufficient to mitigate the danger. Movement evidence was observed, such as the misalignment of trees.

The scar located at Km 493 + 600 (Area 14) is a slope with a rotational landslide scar, which presents variations in soil and weathered gneisses (Figure 8c). The slope showed erosion in the form of grooves and gullies. The cracks in the scars had an extension greater than 1 meter with an opening greater than 5 centimeters. The occurrence of water on the slope was not observed, however the drainage devices found were insufficient, since most of the drainage channels were obstructed. Figure 8d shows the view of the Km 493 + 600 embankment and the rotational landslide scar.

The slope located at Km 482 + 299 (Area 10) is a granite with some portions showing a slight gneissic banding, many quartz veins were observed along the massif (Figure 8e). The soil is sandy. The massif is inserted in the Mantiqueira Complex (CPRM, 2000). The slope presents need for stabilization structures and drainage devices, both of which do not exist in the area (Figure 8f).

3.2. Scar areas estimation using drone and RTK imaging and comparison with estimated areas in Google Earth Pro

Scar areas were measured from images generated by drone imaging and RTK survey, all processed in ArcGis 10.3. For the exposure of the assumptions adopted in the estimations of the studied areas, and better visualization of the processed images, it was taken as an example of analysis the Area 08 (Km 515 + 300) presented in Figure 9.

From the control points, orthomosaics and digital surface models were built. Figure 9 presents a comparison of the spatial resolution of the Area 08 (Km 515 + 300) image obtained in Google Earth Pro for 2016 year and the orthomosaic processed in Pix4D. The better visual quality of the orthomosaic obtained by drone imaging (pixel corresponding to 4.07 centimeters) is clearly observed than the image obtained by Google Earth Pro.
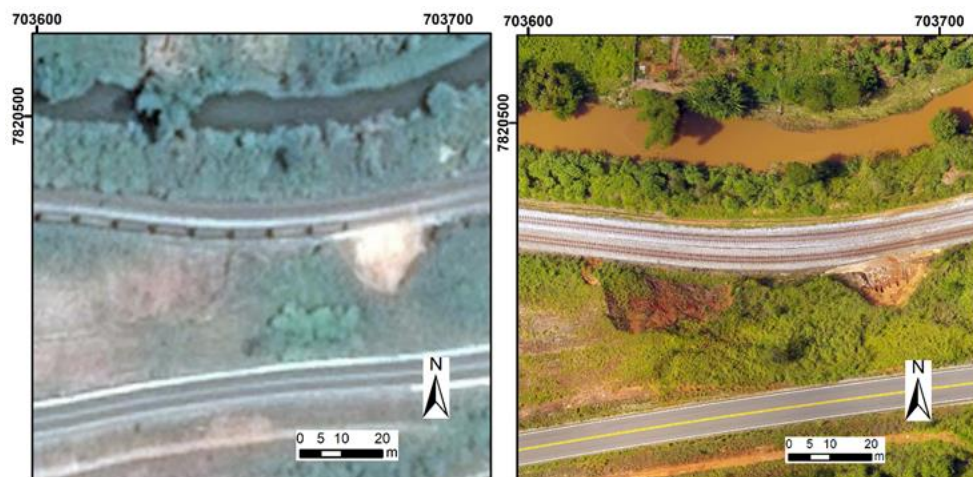

Figure 9. Visual comparison between the spatial resolutions of the Google Earth Pro image and the orthomosaic generated by Pix4D (4.07 cm) from Area 08 (Km 515 + 300).

From the images, it was possible to estimate the scar areas Table 3 presents the results of the estimated areas in both methodologies and their names, as well as the calculation of the values deviation in percentage.

Table 3. Estimated values of scar areas and values deviation obtained between methods.

Strech	Scar	Area from Google Earth Pro (m²)	Area from drone (m²)	Variation (%)
521+000D	Area 01D	1104,83	1198,67	8,49
521+000E	Area 01E	2629,1	2709,89	3,07
518+790	Area 02	1859,05	1947,06	4,73
493+600	Area 04	8174,28	8788,24	7,51
521+522	Area 05	2642,39	3435,51	30,02
520+950	Area 06	2667,65	2965,94	11,18
535+419A	Area 07A	2314,06	1783,24	22,94
535+419B	Area 07B	1490,26	1405,83	5,67
535+419C	Area 07C	541,86	764,25	41,04
515+300A	Area 08A	3668,03	2072,65	43,49
515+300B	Area 08B	274,28	199,25	27,36
513+200	Area 09	13221,65	10644,06	19,5
482+299	Area 10	14047,6	9967,96	29,04
519+900	Area 12	7458,96	8392,73	12,52
524+108	Area 13	2751,04	2936,16	6,73
511+670A	Area 14A	2801,2	2972,95	6,13
511+670B	Area 14B	2900,32	2134,83	26,39
511+670C	Area 14C	2042,83	1661,26	18,68

In order to facilitate the visualization of the results obtained between methods, Figure 10 presents the results of Table 3 in the form of 2 graphs, one of comparison and the other of correlation between the methodologies. From the comparison chart, it is possible to observe that the biggest differences between the two estimates are in the areas 04, 09, 10 and 12, which also present the highest values for the scar areas. This phenomenon can be justified by the quality and/or resolution of the images obtained through Google Earth Pro, which limit the interpretation of scar limits.
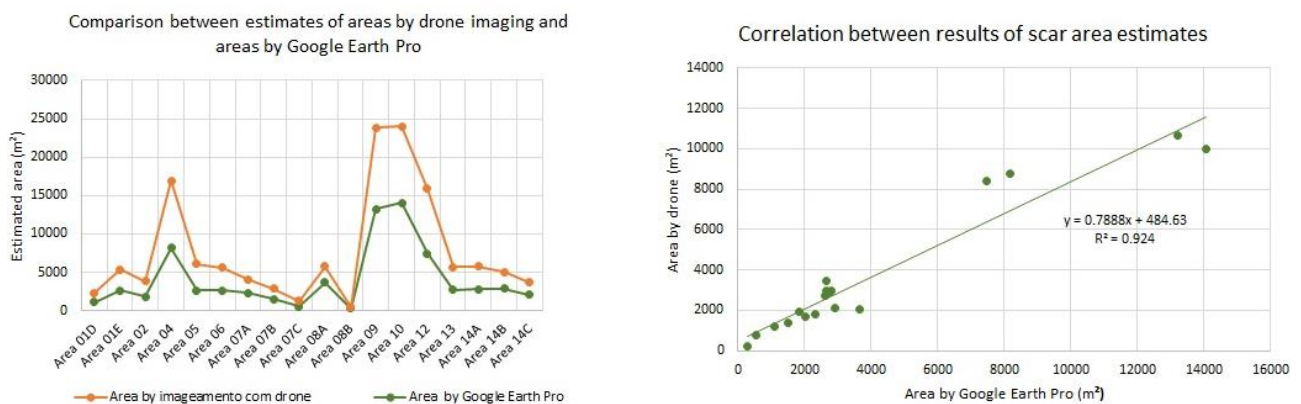
Figure 10. Comparison and correlation between the two methodologies used to estimate scar areas.

In addition, the estimates in both methods show a high degree of correlation, with R² of 0.924, ie 92.4% of the area via Google Earth Pro is explained by the area via drone imaging. This result allows to interpret that Equation 7 can be used to correct the estimate of the area made from the images of Google Earth Pro, allowing to use it as a

tool. This is only possible due to the non-randomness of the differences between the areas obtained by drone imaging and Google Earth Pro, ie the error (difference of results) was constant between the two estimates.

The trend line obtained by the correlation between the results obtained for the two estimation methods is presented in Figure 10 and Eq. (7), where A_I is the area by drone imaging and A_G the area by Google Earth.

$$A_I = 0,7888A_G + 484,63 \tag{7}$$

3.3. Scar volume estimation using drone imaging and RTK and comparison with estimated volumes in Google Earth Pro

In order to estimate the volume generated by the landslides and a greater effectiveness in the accuracy of the results, the characteristics of the scars were determined with the aid of the drone. The next step consisted of processing the data in the Pix4D software. From the point cloud generated in Pix4D it was possible to make the contours of the raised sections using the Global Mapper v17.0 software, to then estimate the scar volumes in the AutoCAD Civil 3D software.

For evaluation purposes, three situations were simulated for volume estimation: minimum volume, represents the situation where the slope ridge coincides with the landslide scar plane; average volume, represents the average situation between the slopes of the maximum volume and the slopes of the minimum volume and maximum volume, characterized by the situation in which the slope has a 90 ° angle.

Thus, in this study, the average volume value was adopted, as this estimate avoids obtaining underestimated or overestimated values. In addition, the average volume was estimated based on the neighboring slopes in the adjacent regions, then approaching the natural topography that existed before. Figure 11a shows the schematic drawing of the pre-event topography construction process and Figure 11b shows the process of estimating the volume mobilized in AutoCAD Civil 3D.
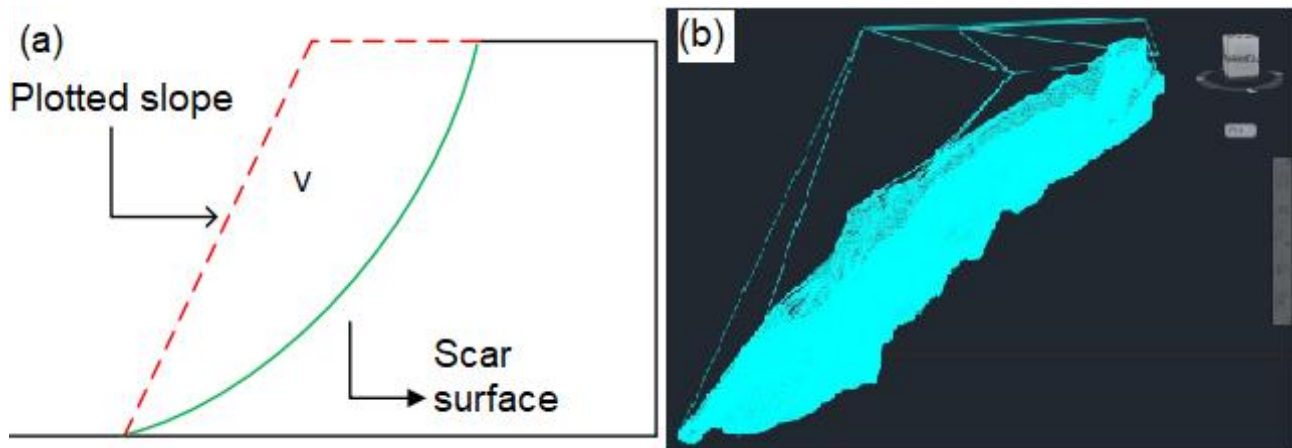
Figure 11. a) Schematic drawing of the pre-event topography construction process. b) Process of estimating the volume mobilized in AutoCAD Civil 3D.

Comparison of scar volume values estimated from Google Earth Pro images and drone imaging is presented in Table 4. Thus, it was possible to correlate the volumes obtained by the two techniques, presented in Figures 12 and discussed below.

Table 4. Comparison between scar volume values obtained by the estimates.

Stretch	Scar	Volume from Google Earth Pro (m³)	Volume from drone (m³)	Variation (%)
521+000D	Area 01D	925,58	1075,45	16,19
521+000E	Area 01E	6057,01	9077,61	49,87
518+790	Area 02	8565,88	14318,97	67,16
493+600	Area 04	70192,69	111367,9	58,66
521+522	Area 05	8301,33	39253,27	372,86

520+950	Area 06	8380,68	14656,41	74,88
535+419A	Area 07A	9693,11	20231,6	108,72
535+419B	Area 07B	6866,63	20908,74	204,5
535+419C	Area 07C	1929,28	5107,38	164,73
515+300A	Area 08A	6914,08	12646,43	82,91
515+300B	Area 08B	574,46	759,92	32,28
513+200	Area 09	60920,99	45604,12	25,14
482+299	Area 10	41189,72	80760,65	96,07
519+900	Area 12	28119,61	47816,28	70,05
524+108	Area 13	4033,24	10348,99	156,59
511+670A	Area 14A	9973,59	18214,63	82,63
511+670B	Area 14B	10326,51	19141,94	85,37
511+670C	Area 14C	5134,19	8686,81	69,2
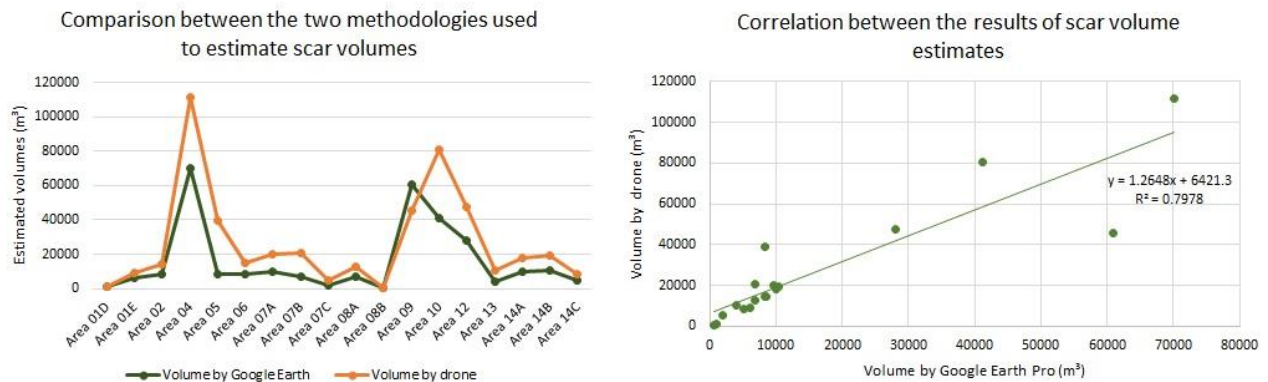
Figure 12. Comparison and correlation between the two methodologies used to estimate scar volumes.

From the analysis of the correlation graph between the two methodologies (Figure 12) it was possible to observe that the results obtained had a correlation of about 80%. Which allows us to interpret that the volume estimate by Google Earth Pro does not present such a satisfactory correlation as for the results obtained in the area calculation, about 92%, when compared to the results obtained with the drone survey.

The estimates that contributed to the decrease in the correlation value were for the points with the highest volume values. This result allows us to conclude that with regard to volume estimation by Google Earth Pro, the higher the volume value the worse the volume estimate will be. In order to observe the differences in the estimates, a comparison was made between the values of the scar volumes obtained by the estimates. The result showed that the volume estimates via drone imaging presented higher values than the volume estimates via Google Earth, except for the Area 09.

Regarding the deviations found between the two estimates (drone x Google Earth Pro) it was observed that the largest deviations occurred in sections that presented higher scar volume values, highlighting the areas 04, 05, 10 and 12, which was expected, due to the size of the scars that causes greater errors in the volume estimates.

4. Conclusions

Two remote sensing techniques were used to collect the geometric parameters, area and volume of the slopes of EFVM, Google Earth Pro and image by drone. Estimates of scars areas using Google Earth Pro and drone imaging showed a high correlation degree, with a R^2 of 0.924. This result allows us to conclude the methodology for estimating areas through Google Earth Pro presents satisfactory results.

However, for the estimates of landslide volume in the scars studied, the methodology used by Google Earth Pro presented values that were underestimated when compared to results obtained by drone imaging. This can be justified by the pixel size of some Google Earth Pro images that can correspond to up to 900 m² (30x30m),

consequently, the volume estimates by the two methods presented a correlation of 0.798; which represents a satisfactory degree of correlation.

This study showed through the relationships obtained that area estimates using Google Earth are more accurate than volume estimates. The high precision and technology in the drone's tools combined with positioning with RTK allow better estimates, but Google Earth is still, currently, a tool more accessible to specialists. Volume estimates through Google Earth can be used, however, carefully, as it was found that the method does not have a good adhesion to the real topographic surface.

Currently, photogrammetric products have gotten space in the market, especially for the easy data acquisition and the large amount of information an aerial image can provide. The use of drones has proved to be an effective and direct geotechnical approach tool for the monitoring and surveying of landslides and, even if it is restricted because of, the different geological sites for large-scale works, such as EFVM, it can contribute to geological risk management. Despite the considerations made, the construction of models for the landslides estimation is not a trivial assignment, because of the number and nature of the qualitative and quantitative variables that are related to this phenomenon.

Referências

1. AVANZI, G. D.; GIANNECCHINI, R.; PUCCINELLI, A. The Influence of the geological and geomorphological settings on shallow landslides. An example in a temperature climate environment: the june 19, 1996 event in northwestern Tuscany (Italy). **Engineering Geology**, v. 73, p. 215-228, 2004. DOI: 10.1016/j.enggeo.2004.01.005

2. BALEK, J.; BLAHUT, J. A critical evaluation of the use of an inexpensive camera mounted on a recreational unmanned aerial vehicle as a tool for landslide research. **Landslides**, v. 14, p. 1217–1224, 2017. DOI: 10.1007/s10346-016-0782-7

3. CARDINALI, M.; REICHENBACH, P.; GUZZETTI, F.; ARDIZZONE, F.; ANTONINI, G.; GALLI, M.; CACCIANO, M.; CASTELLANI, M.; SALVATI, P. A geomorphological approach to estimate landslide hazard and risk in urban and rural areas in Umbria, central Italy. **Natural Hazards and Earth System Sciences**, v. 2 (1–2), p. 57–72, 2002.

4. CHANG-CHUN, L.; GUANG-SHENG, Z.; TIAN-JIE, L.; A-DU, G. Quick image-processing method of UAV without control points data in earthquake disaster area. **Trans Nonferrous Met Soc China**, v. 21, p. 523–528, 2011. DOI: 10.1016/S1003-6326(12)61635-5

5. COLOMINA, I.; MOLINA, P. Unmanned aerial systems for photogrammetry and remote sensing: a review. **ISPRS J Photogramm Remote Sens**, v. 92, p. 79–97, 2014. DOI: 10.1016/j.isprsjprs.2014.02.013

6. CORRÊA, G. P.; KOBIYAMA, M.; GIGLIO, J. N.; MICHEL, G. P.; TASCA, F. A.; GOERL, R. F. Análise geométrica para estimativa de volume em fluxo de detritos. V Seminário Internacional de Defesa Civil (DEFENCIL), 5., 2009, São Paulo. **Anais...** São Paulo: Defesa Civil. 2009. p. 1-10.

7. CORTELETTI, R. C. **Metodologia para análise de riscos geológico-geotécnicos em ferrovias: Estrada de Ferro Carajás (EFC)**, 1ª Ed. Ouro Preto: UFOP, 2017, 222p.

8. CPRM. 2000. Programa Levantamentos Geológicos do Brasil.SE.23-Z-D-IV – Folha Itabira. Carta Geológica, escala 1:100.000.

9. CRUDEN, D. M.; VARNES, D. J. Landslide types and process. In: TURNER, A.K.; SCHUSTER, R.J. (Eds.), **Landslides: Investigation and Mitigation**. Special Report 247. Washington: National Academy Press, 1996. p. 36–75.

10. EISENBEISS, H.; SAUERBIEr, M. Investigation of uav systems and flight modes for photogrammetric applications. **Photogramm Rec,** v. 26(136), p. 400–421, 2011. DOI: 10.1111/j.1477-9730.2011.00657.x

11. FAN, F.; XU, Q. SCARINGI, G.; ZHENG, G, HUANG, R.; DAI, L.; JU, Y. The "long" runout rock avalanche in Pusa, China, on August 28, 2017: a preliminary report. **Landslides**, v. 16, n. 139, p. 139-154, 2018. DOI: 10.1007/s10346-018-1084-z

12. GARCÍA-DELGADO, H.; MACHUCA, S.; MEDINA, E. Dynamic and geomorphic characterizations of the Mocoa debris flow (March 31, 2017, Putumayo Department, southern Colombia). **Landslides**, 16: 597, 2019. DOI: 10.1007/s10346-018-01121-3

13. GALLI, M.; ARDIZZONE, F.; CARDINALI, M.; GUZZETTI, F.; REICHENBACH, P. Comparison of landslide inventory maps. **Geomorphology**, v. 94, p. 268–289, 2008. DOI: 10.1016/j.geomorph.2006.09.023

14. GUNS, M.; VEERLE, V. Shifts in landslide frequency-area distribution after forest conversion in the tropical Andes. **Anthropocene**, v. 6, p. 75-85, 2014. DOI: 10.1016/j.ancene.2014.08.001

15. GUPTA, S. K.; SHUKLA, D. P. Application of drone for landslide mapping, dimension estimation and its 3D reconstruction. **Journal of the Indian Society of Remote Sensing**, v. 46, p. 903-914, 2018. DOI: 10.1007/s12524-017-0727-1

16. GUTHRIE, R. H. The effects of logging on frequency and distribution of landslides in three watersheds on Vancouver Island, British Columbia. **Geomorphology**, v. 43(3–4), p. 273–292, 2002. DOI: 10.1016/S0169-555X(01)00138-6

17. GUTHRIE, R.H.; EVANS, S.G. Analysis of landslide frequencies and characteristics in a natural system, coastal British Columbia. **Earth Surface Processes and Landforms**, v. 29, p. 1321–1339, 2004. DOI: 10.1002/esp.1095

18. GUZZETTI, F.; CARRARA, A.; CARDINALI, M.; REICHENBACH, P. Landslide hazard evaluation: a review of current techniques and their application in a multi-scale study. **Geomorphology**, v. 31, p. 181–216, 1999. DOI: 10.1016/S0169-555X(99)00078-1

19. GUZZETTI, F.; REICHENBACH, P.; CARDINALI, M.; GALLI, M.; ARDIZZONE, F. Probabilistic landslide hazard assessment at the basin scale. **Geomorphology**, v. 72, p. 272–299, 2005. DOI: 10.1016/j.geomorph.2005.06.002

20. GUZZETTI, F.; ARDIZZONE, F.; CARDINALI, M.; GALLI, M.; REICHENBACH, P.; ROSSI, M. Distribution of landslides in the Upper Tiber River basin, central Italy. **Geomorphology**, v. 96, p. 105–122, 2008. DOI: 10.1016/j.geomorph.2007.07.015

21. GUZZETTI, F.; ARDIZZONE, F.; CARDINALI, M.; ROSSI, M.; VALIGI, D. Landslide volumes and landslide mobilization rates in Umbria, central Italy. **Earth and Planetary Science Letters**, v. 279(3–4), p. 222–229, 2009. DOI: 10.1016/j.epsl.2009.01.005

22. GUZZETTI, F.; MONDINI, A.C.; CARDINALI, M.; FEDERICA, F.; SANTANGE, M.; CHANG, K.T. Landslide inventory maps: New tools for an old problem. **Earth-Science Reviews**. v. 112, p. 42–66, 2012. DOI: 10.1016/j.earscirev.2012.02.001

23. HOVIUS, N.; STARK, C. P.; ALLEN, P. A. Sediment flux from a mountain belt derived by landslide mapping. **Geology**, v. 25, p. 231–234, 1997. DOI: 10.1130/0091-7613(1997)025<0231:SFFAMB>2.3.CO;2

24. IMAIZUMI, F.; SIDLE, R.C. Linkage of sediment supply and transport processes in Miyagawa Dam catchment, Japan. **Journal Geophysical Research**, v. 112 (F03012), 2007. DOI: 10.1029/2006JF000495

25. IMAIZUMI, F.; SIDLE, R.C.; KAMEI, R. Effects of forest harvesting on the occurrence of landslides and debris flows in steep terrain of central Japan. **Earth Surface Processes and Landforms**, v. 33, p. 827–840, 2008. DOI: 10.1002/esp.1574

26. INNES, J. N. Lichenometric dating of debris-flow deposits in the Scottish Highlands. **Earth Surface Processes and Landforms**, v. 8, p. 579–588, 1983. DOI: 10.1002/esp.3290080609

27. IVERSON, R. M.; GEORGE, D. L.; ALLSTADT, K.; REID, M. E.; COLLINS, B. D.; VALLANCE, J. W.; S. P. SCHILLING, J. W. GODT, C. M. CANNON, C. S. MAGIRL, R. L. BAUM, J. A. COE, W. H. SCHULZ,

BOWER, J. B. Landslide mobility and hazards: Implications of the 2014 Oso disaster. **Earth and Planetary Science Letters**, v. 412, p. 197–208, 2015. DOI: 10.1016/j.epsl.2014.12.020

28. JAMES, M. R.; ROBSON, S. Straightforward reconstruction of 3D surfaces and topography with a camera: accuracy and geoscience application, **J Geophys Res**, v. 117, p.03-17, 2012. DOI: 10.1029/2011jf002289

29. KARKI, K.; SULTAN, M.; AL-SEFRY, S. A.; ALHARBI, H. M.; EMIL, M. K.; ELKADIRI, R.; ALFADAIL, E. A. A Remote Sensing–based Intensity-Duration Curve, Faifa Mountains, Saudi Arabia. **Nat. Hazards Earth Syst. Sci. Discuss**. 2018. DOI: 10.5194/nhess-2018-282

30. KENNEDY, D.; BISHOP, M.C. Google Earth and the archaeology of Saudi Arabia. A case study from the Jeddah area. **Journal of Archaeological Science**, v. 38 (6), p.1284-1293, 2011. DOI: 10.1016/j.jas.2011.01.003

31. KORUP, O. Distribution of landslides in southwest New Zealand. **Landslides**, v. 2, p. 43–51, 2005. DOI: 10.1007/s10346-004-0042-0

32. LEE, S.; CHWAE, U.; KYUNGDUCK M. Landslides susceptibility mapping by correlation between topography and geological structure: the Janghung area, Korea. **Geomorphology**, v. 46, p.149-162, 2002. DOI: 10.1016/S0169-555X(02)00057-0

33. LEE, Y. F. E CHI, Y.Y. Rainfall-induced landslide risk at Lushan, Taiwan. **Engineering Geology,** v. 123, p. 113–121, 2011. DOI: 10.1016/j.enggeo.2011.03.006

34. LOPES, E. E. **Proposta Metodológica para Validação de Imagens de Alta Resolução do Google Earth para a Produção de Mapas**. Dissertação (Mestrado em Engenharia Civil) – Programa de Pós-Graduação em Engenharia Civil – Universidade Federal de Santa Catarina, Florianópolis. 2009, 127p.

35. MALAMUD, B. D.; TURCOTTE, D. L.; GUZZETTI, F.; REICHENBACH, P. Landslide inventories and their statistical properties. **Earth Surface Processes and Landforms**, v. 29, p. 687–711, 2004. DOI: 10.1002/esp.1064

36. MENDONÇA, F. B.; DINIZ, N. C.; BAPTISTA G. M. M. Mapa de risco de movimentos gravitacionais de massa, obtidos por meio de inventário de cicatrizes de deslizamentos no trecho 4 do trem de alta velocidade brasileiro. **Rev. Bras. De Geologia de Engenharia e Ambiental**, São Paulo, p. 73 – 94, 2012.

37. PARCAK, S. H. **Satellite Remote Sensing for Archaeology**. 1ª Ed. Londres: Routledge Press, 2009, 320p.

38. PANIZZA, A. C.; FONSECA, F. P. Técnicas de Interpretação Visual de Imagens. **GEOUSP- Espaço e Tempo**, São Paulo, v. 30, p. 30 – 43, 2011.

39. PEPPA, M. V.; MILLS, J. P.; MOORE, P.; MILLER, P. E.; CHAMBERS, J. E. Brief communication: landslide motion from cross correlation of UAV-derived morphological attributes. **Nat Hazards Earth Syst Sci**, v. 17, p. 2143–2150, 2017. DOI: 10.5194/nhess-17-2143-2017

40. PEROTTO-BALDADIVIEZO, H. L.; THUROW, T. L.; SMITH C. T.; FISHER, R. F.; WU, X. B. Gis Based Spatial analysis and modelling for landslides hazard assessment in steeplands, southern Honduras. **Agriculture, Ecosystems and Enviromental**, v. 103(1), p. 165-176, 2004. DOI: 10.1016/j.agee.2003.10.011

41. PETERNEL, T.; KUMELJ, S.; OSTIR, K.; KOMAC, M. Monitoring the Potoška planina landslide (NW Slovenia) using UAV photogrammetry and tachymetric measurements. **Landslides**, v. 14, p. 395–406, 2017. DOI: 10.1007/s10346-016-0759-6

42. POLANCO, L. S. E. **Correlações Empíricas para Fluxo de Detritos** (Master Thesis). UFRJ, Rio de Janeiro, Brazil, 2010, 110 p.

43. REICHENBACH, P.; GALLI, M.; CARDINALI, M.; GUZZETTI, F.; ARDIZZONE, F. (2005). Geomorphologic mapping to assess landslide risk: concepts, methods and applications in the Umbria Region of central Italy. In: GLADE, T.; ANDERSON, M.G.; Crozier, M.J. (Eds.), **Landslide Risk Assessment**, 1ª Ed. John Wiley, Chichester, p. 429–468. DOI: 10.1002/9780470012659.ch15

44. RICE, R. M.; CORBETT, E. S.; BAILEY, R. G. Soil slips related to vegetation, topography, and soil in Southern California. **Water Resources Research,** v. 5 (3), p. 647–659, 1969.

45. ROSSI, G.; NOCENTINI, M.; LOMABRDI, L.; VANNOCCI, P.; TANTERI, L.; DOTTA, G.; BICOCCHI, G.; SCADUTO, G.; SALVATICI, T.; TOFANI, V.; MORETTI, S.; CASAGLI, N. Integration of multicopter drone measurements and ground-based data for landslide monitoring. In: AVERSA, S.; CASCINI, L.; PICARELLI, L.; SCAVIA, C. (Eds.). **Landslides and Engineered Slopes. Experience, Theory and Practice**. 1ª Ed. Napoli: CRC Press, 2016. p. 1745-1750. DOI: 10.1201/9781315375007-206

46. ROSSI, G.; TANTERI, L.; TOFANI, V.; VANNOCCI, P.; MORETTI, S.; CASAGLI, N. Multitemporal UAV surveys for landslide mapping and characterization. **Landslides**, v. 15(5), p. 1045–1052, 2018. DOI: 10.1007/s10346-018-0978-0

47. SADR, K.; RODIER, X. Google Earth, GIS and stone-walled structures in southern Gauteng, South Africa. **Journal of Archaeological Science**, v. 39 (4), p. 1034-1042, 2012. DOI: 10.1016/j.jas.2011.11.024

48. SILVA, D. C.; TOONSTRA, G. W. A.; SOUZA, H. L. S.; PEREIRA, T. A. J. Qualidade de Ortomosaicos de Imagens de Vant processados Com os Softwares APS, PIX4D e PHOTOSCAN. In: V Simpósio Brasileiro de Ciências Geodésicas e Tecnologias da Geoinformação, 5., 2014, Recife. **Anais...** Recife: UFPE. 2014. p. 747-756.

49. SILVA, D. F. S.; SANTOS, A. E. M.; FERREIRA, B. T.; PEREIRA, T.M.; CORTELETTI, R. C. Cluster analysis for slope geotechnical prioritization of intervention for the Estrada de Ferro Vitória-Minas. **REM - International Engineering Journal**, v. 71(2), p. 167-173, 2018. DOI: 10.1590/0370-44672017710173

50. SIMONETT, D. S. (1967). Landslide distribution and earthquakes in the Bewani and Torricelli Mountains, New Guinea. In: JENNINGS, J.N.; MABBUTT, J.A. (Eds.), **Landform Studies from Australia and New Guinea**. 1ª Ed. Cambridge University Press, Cambridge, p. 64–84.

51. TEN BRINK, U. S.; GEIST, E. L.; ANDREWS, B. D. Size distribution of submarine landslides and its implication to tsunami hazard in Puerto Rico. **Geophysical Research Letters,** v. 33, p. 1-4, 2006. DOI: 10.1029/2006GL026125

52. TRAVELLETTI, J.; DELACOURT, C.; ALLEMAND, P.; MALET, J. P.; SCHMITTBUHL, J.; TOUSSAINT, R.; BASTARD, M. Correlation of multi-temporal ground-based optical images for landslide monitoring: application, potential and limitations. **ISPRS J Photogramm Remote Sensor**s v. 70, p. 39–55, 2012. DOI: 10.1016/j.isprsjprs.2012.03.007

53. TURNER, D.; LUCIEER, A.; JONG, S. M. Time series analysis of landslide dynamics using an unmanned aerial vehicle (UAV). **Remote Sensors**, v. 7, p. 1736–1757, 2015. DOI; 10.3390/rs70201736

54. VALAGUSSA, A.; MARC, O.; FRATTINI, P.; CROSTA, G. B. Seismic and geological controls on earthquake-induced landslide size. **Earth and Planetary Science Letters**, v. 506, p. 268–281, 2019. DOI: 10.1016/j.epsl.2018.11.005

55. VALE (2017). **Sobre a Vale. Notícias**. Disponível em: <http://www.vale.com/brasil/PT/aboutvale/news/Paginas/ferrovia-vitoria-minas-transportou-119-milhoes-to neladas-cerca-1-milhao-pessoas-2014.aspx>. Accessed in: jan. 2017.

56. VANACÔR, R. N. **Sensoriamento Remoto e Geoprocessamento aplicados ao mapeamento das áreas susceptíveis a movimentos de massa na região nordeste do Estado do Rio Grande do Sul**. Dissertação (Mestrado em Sensoriamento Remoto) – Programa de Pós-Graduação em Sensoriamento Remoto, Universidade Federal do Rio Grande do Sul, Porto Alegre. 2006. 132p.